THE IMPACT OF SAMPLE TILT ON SCANNING TRANSMISSION ELECTRON MICROSCOPY IN STRONTIUM TITANATE

A Thesis

Presented to the Faculty of the Graduate School

of Cornell University

in Partial Fulfillment of the Requirements for the Degree of

Master of Science

by

Colin R. Bundschu

May 2018

ABSTRACT

Annular Bright Field Scanning Transmission Electron Microscopy (ABF-STEM) allows microscopers to image the location of atoms in films as thin as a single atomic layer. In high signal to noise images sub-picometer localization precision is achievable. Recent work has used ABF-STEM to measure oxygen displacements in complex oxides heterostructures, with intent of showing ferromagnetic and multiferroic properties. However, previous work on the accuracy of ABF-STGEM imaging has shown that when a sample is tilted by $6\,\mathrm{mrad}$ relative to the electron beam, it creates artificial displacements of $11.9\,\mathrm{pm}$ between oxygen and cation columns [11]. Artifacts of this magnitude make picometer-scale measurements of oxygen displacements impossible. However, use of Convergent Beam Electron Diffraction (CBED) can aid sample alignment in the STEM and mistilts can typically be reduced to approximately $1\,\mathrm{mrad}$ or better.

Thus, there remains an open question as to what kinds of tilt-induced artifacts exist at sample tilts expected in experimental ABF-STEM. In order to quantify the effects of a sample tilt of $1\,\mathrm{mrad}$, I performed multislice image simulations on cubic $SrTiO_3$ over a range of thicknesses from one atomic layer to just over $30\,\mathrm{nm}$. I found that even with only $1\,\mathrm{mrad}$ of tilt, artificial displacements so large as $11.8\,\mathrm{pm}$ between titanium/oxygen and oxygen columns and $4.2\,\mathrm{pm}$ between strontium and titanium/oxygen columns are present in ABF-STEM images. I further found that these displacements are not present in HAADF-STEM images, as the displacement between strontium and titanium/oxygen columns was below $0.2\,\mathrm{pm}$ at $1\,\mathrm{mrad}$ of sample tilt and less than $1.5\,\mathrm{pm}$ at sample tilts up to $10\,\mathrm{mrad}$. Because tilts of this magnitude are difficult to control for experimen-

tally, the apparent location of atomic positions in ABF-STEM images may not accurately reflect true atomic structure and measurements of picometer-scale oxygen distortions in complex oxides may not be possible unless sample tilt is carefully controlled.

BIOGRAPHICAL SKETCH

Colin Bundschu graduated from Harvey Mudd College in 2013 with a B.S. in Computer Science. He then worked for Microsoft Game Studios as a software engineer, having a hand in the launch of the Xbox One. Afterwards, he worked for Rockstar Games on Red Dead Redemption 2 as a game designer. Subsequently, he worked for Oculus Virtual Reality, a Facebook subsidiary, as a software engineer working on the launch of the Oculus Rift, one of the first commercially available Virtual Reality headsets.

In 2016 he left the videogame industry to pursue a master's degree in Applied and Engineering Physics at Cornell. Starting in the fall of 2018, he will begin a PhD in the same department.

This document is dedicated to all Cornell graduate students.

ACKNOWLEDGEMENTS

I'd like to thank my advisor, Dr. Lena Kourkoutis, for her support of my research at Cornell as a master student. Her guidance has been invaluable in starting my career as a researcher, and I am deeply appreciative for the time and energy she invested in me as a student. When I came to her group I had little more than a junior level understanding of physics, and she helped me become the scientist I am today.

I'd also like to thank Dr. Earl Kirkland for developing the multislice software used to make my simulations, for assisting me with making careful multislice calculations, and for being an excellent instructor. I eagerly look forward to his wit and humor as I continue graduate studies at Cornell.

Many thanks to Dr. Joel Brock for running the master student seminar and providing advice to me as I figured out my future plans. His mentorship was an invaluable step on my way to starting a doctorate, and he is one of the most supportive professors in the department.

I'd like to thank my labmates for their help in getting up to speed in electron microscopy so that I could do my research. Special thanks to Ismail El Baggari who was essential in me getting up to speed with multislice.

I'd further like to thank Mari Tader for her assistance in editing and proofreading this thesis. She must have read this document half a dozen times, and I'm appreciative for her excellent writing skills.

Finally, I would like to thank my parents for their support in getting me here today. Their love and support has been the greatest asset in achieving my goals.

TABLE OF CONTENTS

LIST OF FIGURES

CHAPTER 1

INTRODUCTION

1.1 Motivation and Previous Work

1.1.1 Motivation for Electron Microscopy

Many interesting material properties only emerge at the nanoscale or are fundamentally due to microscopic variations. To characterize and understand these effects, in order to build devices that utilize them, we need to be able to see materials at the atomic level.

Unfortunately, light microscopy is unable to perform atomic-scale imaging. The diffraction limit of visible light sets a minimum on the size of objects able to be resolved with an optical microscope. This limit is commonly given by the Abbe formula (Eq. 1.1) where d is the minimum resolvable distance, λ is the wavelength of light, n is the refractive index of the material the light is travelling through, and θ is the aperture half-angle of the lens [28]. Typically, the $n \sin\theta$ term is replaced with a value called the numerical aperture (NA). NA represents the angular range within which an objective can transmit or accept light in a given medium, and thus how finely the lens can resolve objects at a distance. Using a medium of high index of refraction such as immersion oil ($n = 1.52$) [32], and noting that $\sin\theta$ can reach a maximum value of 1, we can achieve a NA of approximately 1.5. Using light with a wavelength of $500\,\mathrm{nm}$ allows us to resolve features of approximately $167\,\mathrm{nm}$. This resolution is several orders of magnitude too large for resolving individual atoms, which have length scales

on the order of one Angstrom.

$$d = \frac{\lambda}{2n \sin \theta} = \frac{\lambda}{2\mathrm{NA}} \tag{1.1}$$

One method to overcome the diffraction limit of visible light is to use radiation with smaller wavelengths, such as x-rays. However, the Planck-Einstein relation states that the energy of a photon is directly proportional to its wavelength (Eq. 1.2) [13], so as we decrease the wavelength of our imaging radiation, we impart more energy into the imaged sample per photon. As such imaging atomic-scale features using x-rays incurs significant radiation damage in materials robust to radiation damage and completely obliterates organic molecules [18]. While research on femtosecond x-ray pulses and nanometer-scale beams is underway to tackle this challenge, conventional diffraction techniques make atomic scale x-ray imaging impossible in most materials [5, 20, 33].

$$E = \frac{hc}{\lambda} \tag{1.2}$$

An ideal solution to the diffraction limit would be an imaging technique with a small wavelength and low dosing requirements, which has led to the rise of electron microscopy. While electrons are subject to the same diffraction limit as electromagnetic radiation, for many samples an image can be generated with less radiation damage using electrons versus x-rays. The advantage of electrons comes from the fact that relatively few electrons need to be fired at a sample to generate an image. This need is due to strong scattering effects of electrons off of atomic nuclei and ease of detection using scintillators and direct electron detectors [31].

1.1.2 Scanning Transmission Electron Microscopy (STEM)

In order to take advantage of the benefits of electrons, several imaging techniques have been developed. One of these is Transmission Electron Microscopy (TEM). TEM is a form of electron microscopy where electrons are accelerated through a voltage potential and transmitted through a thin sample. The transmitted electrons are then diffracted onto a detector [39]. The strong interactions of electrons with atomic potentials makes this technique an ideal choice for imaging thin films [34, 10] and material interfaces [17], which can be prepared for imaging by milling down a large sample to nanometer thicknesses [4, 26].

Scanning Transmission Electron Microscopy (STEM) is a further refinement on the TEM imaging technique. In this imaging mode, magnetic lenses focus electrons to a narrow point on the sample, called a probe. This probe is then raster scanned across the sample in a 2D grid. Detectors are placed at various geometries which collect electrons scattered from atoms in the sample. At each probe position, the electron intensity on each detector is integrated to create a pixel for the final image. The collection of these pixels is a 2D, real-space image with resolution given by the probe size, probe positioning, and the interaction of the electrons with the sample [39].

Compared to conventional TEM, in STEM information is collected one pixel at a time. The scattering geometry affords flexibility in detector placement and a range of signals can be collected, some even simultaneously. Typically in STEM an annular detector is placed outside of the exiting electron beam, called the dark field region. Because this detector is a located at a larger angle than the aperture of the focused electron probe, the signal is only strong when the probe

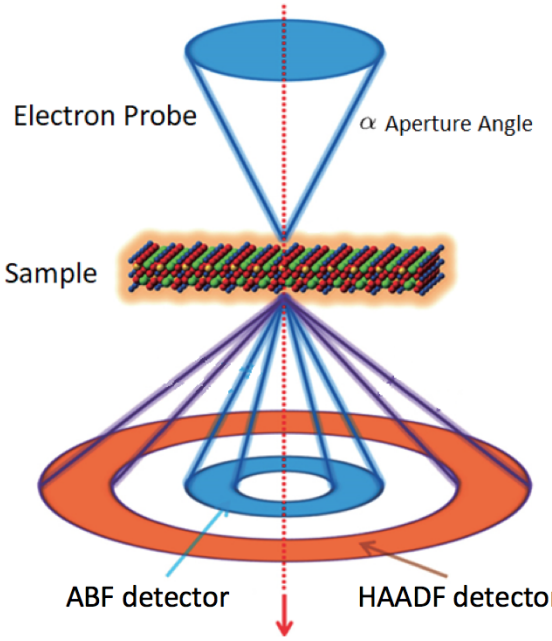

Figure 1.1: An electron microscope in STEM mode. The probe is swept in a 2D grid across the sample. Each probe position generates one pixel of information in the STEM image per detector. Image Source: Zhang et al. [41]

is over an atom, which causes electrons in the probe to scatter to the detector elastically. This causes atoms to appear white on a dark background. This type of detector is called an Annular Dark Field (ADF) detector. Detectors with large inner angle (typically $\tilde{3}$x the probe forming aperture) are referred to as high angle (HA)ADF. Detectors can also be placed at a lower angle than the aperture of the beam. In this setup atoms scatter electrons away from the detector, causing atoms to appear dark on a white background. An annular version of this detector, typically covering angles from half the probe aperture to the full probe aperture, is called an Annular Bright Field (ABF) detector. A depiction of a typical STEM imaging setup containing both a HAADF and an ABF detector is shown in Figure 1.1. A detailed comparison of these detector setups is presented in Section 1.1.3.

1.1.3 Comparison of Annular Bright Field (ABF) vs. High Angle Annular Dark Field (HAADF) Imaging Modes

Electrons scattered to high angles are electrons that are elastically scatter by Rutherford Scattering from the atoms in the sample. Because the scattering is incoherent, phase information is not present in the image, and images made from these electrons can be directly interpreted as atomic structure. Since this scattering has Z^2-dependence, only the heaviest atoms in a material are imageable as lighter atoms do not generate a strong enough signal to be detectable over background noise. In this imaging mode atoms appear white on a black background. This is the region where the High Angle Annular Dark Field (HAADF) detector is placed.

The other region is the bright field, or the region that is in the path of the exiting beam. As the beam propagates through a sample, atoms scatter electrons away from the detector. Thus, to first approximation, signal is reduced when atomic columns are between the probe and the detector, and as such atoms appear dark on a light background. Since heavier atoms scatter more strongly, they appear darker, but because we measure the subtracted signal, both heavy and light atoms are imageable. However, for ABF imaging, coherence has to be considered and phase information is present in the final image. This causes atoms to oscillate between being light and dark as a function of thickness due to interference.

Since both the HAADF and ABF detectors are annular detectors and have non-overlapping angles, they can be used simultaneously.

1.1.4 Motivation for Annular Bright Field (ABF) Imaging

Historically, STEM imaging has been done using HAADF detectors. The STEM imaging technique was first developed in 1938 by Baron Manfred von Ardenne, but his initial STEM microscope did not improve upon TEM microscopes at the time [12]. However, the development of the field emission gun and the addition of a high quality objective lens by Albert Crewe led to the creation of the first modern STEM microscope, which utilized a HAADF detector [8]. Thanks to continued improvements in lenses, by the late 1980's resolution improved to the point atomic structures could be imaged with $2\,\text{Å}$ of resolution [36]. With the addition of aberration correctors in the 1990's, electron probes could be further focused to sub-Angstrom diameters, improving HAADF resolutions and allowing detection of individual atomic columns with picometer-scale precision [3, 9, 15].

The direct interpretability and relative robustness of HAADF imaging made it a strong choice for early modern STEM setups and continue to make it a strong choice today. However, because light atoms are not visible in HAADF images of materials that also contain heavy atoms, interest in ABF imaging has grown among researchers studying thin film complex oxides.

Interest in thin film complex oxides exists in part because this class of materials hosts a range of fundamentally and technologically interesting phenomenon such as a ferroelectricity, metal insulator transitions, and superconductivity. Many of these phenomena critically depend on the atomic structure.In addition, epitaxial strain induced by growing an oxide with slightly different lattice constants on an oxide substrate can induce structural distortions which alters the film properties.

With the development of pulse-laser deposition and molecular beam epitaxy, innumerable possible combinations of films and substrates can be grown with relative ease. As such, researchers seek to engineer interfaces with desired properties by carefully choosing substrate and film materials. In order to confirm that they have developed the material they are going after, these researchers turn to ABF-STEM imaging to image their results.

Already, many scientists have used ABF-STEM imaging to make picometer scale measurements of complex oxide interfaces. Tan et al. used ABF-STEM to make bond angle measurements of S–Mo–S in monolayer MoS_2 films. When these films are bent, they can be used to catalyze hydrogen evolution reactions (HER) for electrocatalytic hydrogen production [37]. Kan et al. used ABF-STEM to measure Ru–O–Ti and Ru–O–Ru bond angles at the interface of $SrRuO_3$ and $Ca_{0.5}Sr_{0.5}TiO_3$ with claimed sub-Angstrom precision as a proof of concept for demonstrating the ability to control the shape of oxygen octahedrals in $SrRuO_3$ by varying the thickness of the grown $Ca_{0.5}Sr_{0.5}TiO_3$ [22]. The bond angle measurements of oxygen octahedrals in their paper show differences on the order of $10°$, and picometer-scale precision is needed to quantify bond angles differences at that level in this material. Ovsyannikov et al. measured Mn–O–Mn angles in perovskite–type ζ-Mn_2O_3 that they synthesized, demonstrating possible ferromagnetic, multiferroic, and colossal magnetoresistive properties [35]. These angles required picometer scale precision in both manganese and oxygen sites to accurately characterize. Kvit et al. measured strain in $LaMnO_3$ by measuring the bond angles of cation columns with claimed sub-picometer precision using a combination of HAADF and ABF imaging techniques [25]. Haas et al. made sub-picometer HAADF measurements of inversion domain boundaries in GaN, with qualitative support from ABF imaging [14]. GaN domain bound-

aries are defects that modify the luminescence of the material, and their results show a deviation from theoretical models of how they should behave. Aso et al. used ABF-STEM to quantify the oxygen octahedral rotations in $ATiO_3/GdScO_3$, where the 'A' represents barium or various ratios of strontium and calcium [1]. They showed that rotations in the oxygen octahedral at the interface were larger when small A-site cations were used, citing error bars less than $5°$ in the angle of the tilt. The measurement of oxygen tilt angles this precisely requires picometer-scale measurements of oxygen positions. Liao et al. made measurements of oxygen octahedral rotations at the interface of a $La_{2/3}Sr_{1/3}MnO_3$ thin film on a $NdGaO_3$ substrate with tilt error bars of approximately $5°$, which would require picometer scale precision [27]. Demand for characterizing rotations in the oxygen octahedral in perovskite structures is strong enough that scientists have developed generalized tools for characterizing them. Weng et al. developed a software tool that can extract oxygen octahedra measurements from experimental HAADF-STEM images with $3\,\mathrm{pm}$ precision and measurements from ABF-STEM images with $4\,\mathrm{pm}$ of precision [38]. He et al. developed a methodology for characterizing the shape of octahedral rotations by comparing experimental ABF images to simulations in $CaTiO_3$ grown on a $(LaAlO_3)_{0.3}(Sr_2AlTaO_6)_{0.7}$ substrate [16].

Despite this increasingly widespread use of ABF-STEM imaging for picometer scale measurements, there is strong evidence that ABF-STEM imaging is sensitive to tilt-induced artifacts. Maccagnano et al. and Yu et al. found that the brightness of atomic columns decreases as the tilt angle increases, causing a reduction of a half with 1 degree of tilt [30, 40]. Gao et al. used multislice simulations in comparison with experimental images to study tilt-induced artifacts in ABF-STEM imaging. Their findings indicate that a $6\,\mathrm{mrad}$ sample tilt

relative to the beam axis can cause an artificial displacement of $11.9\,\mathrm{pm}$ between anion and cation positions under typical experimental conditions for cubic STO. They further demonstrate that probe aperture, sample thickness, probe defocus, and tilt angle all have a substantial effect on the tilt induced column displacement. Zhou et al. did a detailed simulation of the effects of sample tilt on ZrO_2 and found that $1\,\mathrm{mrad}$ sample tilt relative to the beam axis created multiple picometer displacements in oxygen and up to $2\,\mathrm{pm}$ displacements in Zirconium columns [42].

Both Zhou and Gao's results are a powerful demonstration of the effects of tilt on ABF image formation. However, simulations for cubic STO with sample tilts of around $1\,\mathrm{mrad}$ have not been investigated yet. Since these tilt angles are similar to experimental ones, a focused investigation of STO with tilt of this magnitude is needed. Furthermore, since much of ABF-STEM imaging is performed at room temperature, the effects of thermal vibrations on tilt-induced column displacements are relevant. In this paper I investigate these effects to better understand the effects of $1\,\mathrm{mrad}$ tilt on STO.

1.2 Multislice Simulation of STEM Images

In order to simulate the effects of tilt on HAADF and ABF image formation, I used Dr. Earl Kirkland's multislice simulation software as presented in *Advanced Computing in Electron Microscopy* [23].

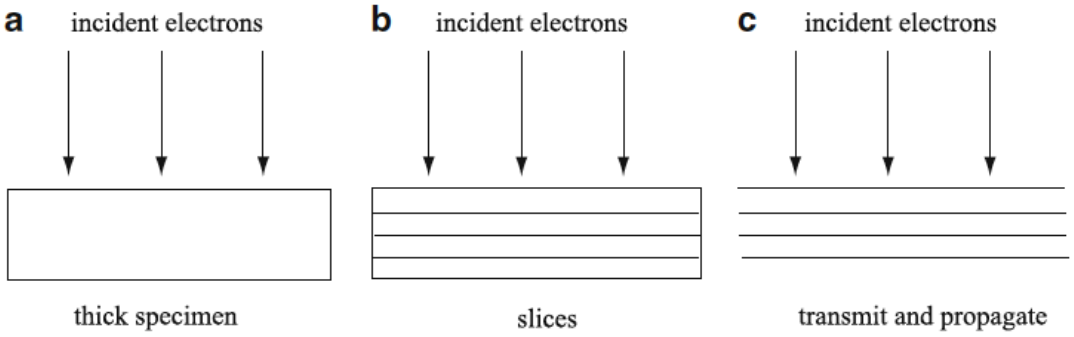

Figure 1.2: A thick specimen is split into several layers for multislice simulation. a) The initial sample b) The sample is sliced into thin layers. c) The electrons are transmitted through atoms and propagated through free space between them. Image Source: Kirkland [23]

1.2.1 Algorithm

In this paper, I simulated STEM images in thick (meaning greater than a few atoms thick) specimens. This section summarizes the algorithm used to do this, which is implemented by Kirkland and documented in *Advanced Computing in Electron Microscopy* [23].

At a high level, multislice works by dividing a thick sample into thin slices and propagating electrons between them. At the end the electrons exit the sample and are projected onto a detector. This process is performed for each pixel in the image, and is depicted in Figure 1.2.

In detail, the multislice algorithm works as follows. First, the specimen is partitioned into slices exactly one half unit cell thick (1.9525 Angstroms for STO). This ensures slice boundaries are centered on atomic potentials in the STO lattice. At the boundary between each slice, the total specimen potential $v_z(\vec{x})$ (Eq. 1.3) is generated by projecting a linear combination of atomic poten-

tials (each given by $v_{zj}(\vec{x}-\vec{x}_j)$) onto the plane of the slice boundary. Combining atomic potentials in a linear manner like this is not completely accurate, as it neglects the effects of bonding on electronic structure. However, without full DFT calculations, such bonding structure is not known. For high-angle imaging, i.e. the kind used with a HAADF detector, the effect of bonding on the electron scattering is small enough to be neglected. For low angle scattering, i.e. the kind picked up by an ABF detector, the exact magnitude of the error is not known, although it has been posited to be on the order of 5% to 10% by extrapolating from x-ray diffraction experiments [23].

$$v_z(\vec{x}) = \sum_{j=1}^{N} v_{zj}(\vec{x}-\vec{x}_j) \tag{1.3}$$

Since each slice is a single atomic layer thick, and the electron probe wavefunction is a linear combination of plane waves, we can account for the interaction of the incoming electron with the material as a change of phase in each of the plane waves comprising the wavefunction. We do this using a transmission function $t(\vec{x})$ (Eq. 1.4), which is multiplied by the probe wave function $\psi(\vec{x})$ to generate the transmitted probe wave function $\psi_t(\vec{x})$.

$$t(\vec{x}) = \exp[i\sigma v_z(\vec{x})] \tag{1.4}$$

Note that in Eq. 1.4, σ is the interaction parameter of the electron with the atomic potential of material at the current layer (Eq. 1.5). For this form to be valid, the specimen potential must be much smaller than the beam energy, which would be true experimentally [23].

$$\sigma = \frac{2\pi\gamma m_0 e\lambda}{h^2} \tag{1.5}$$

Finally, we propagate the transmitted wave function through space to the next slice, which is done by convolving it with a free space propagator $p(x, y, \Delta z)$ in the x and y directions. The propagator is given by (Eq. 1.6):

$$p(x, y, \Delta z) = \mathcal{F}^{-1}[P(k, \Delta z)] = \frac{1}{i\lambda\Delta z} \exp[\frac{i\pi}{\lambda\Delta z}(x^2 + y^2)] \tag{1.6}$$

Taking the convolution of this with the transmitted probe wavefunction gives us a the incident probe wavefunction for the next layer, $\psi_{n+1}(x, y)$ (Eq. 1.7):

$$\psi_{n+1}(x, y) = p(x, y, \Delta z) \otimes [t_n(x, y)\psi_n(x, y)] + \mathcal{O}(\Delta z^2) \tag{1.7}$$

Since our sampling is discrete, in practice we calculate this convolution efficiently using a Fast Fourier Transform (FFT) (Eq. 1.8) [21]:

$$\psi_{n+1}(x, y) = \mathcal{F}^{-1}[P(k_x, k_y, \Delta z)\mathcal{F}[t_n(x, y)\psi_n(x, y)]] + \mathcal{O}(\Delta z^2) \tag{1.8}$$

Once the wavefunction is propagated all the way through the sample, another FFT is performed to diffract the wavefunction into the far field. The square modulus of the wavefunction in the diffraction plane is then integrated over the region of the detector to generate the total intensity of the pixel for that probe position. The combination of the pixels forms a 2D image with the same resolution as the sampling grid of the probe, and is our output STEM image.

Note that this overview does not discuss various anti-aliasing techniques that are used. Importantly, when performing the FFT's described, one must bandwidth limit the signal to only be within a cylindrically symmetric shell within the sample crystal. This is because the probe is fundamentally cylindrically symmetric, and as such not properly clipping the corners of the super cell will introduce rectangular artifacts in the final image.

1.2.2 Tilt Approximation

Sample tilt is approximated by modifying the propagator function for the multislice simulation algorithm. Rather than tilting the actual sample or the beam, both are kept in alignment. Instead, for small angles we can modify the propagator function (Eq. 1.6) to include a tilt (Eq. 1.9), where θ_x and θ_y are the tilts in the x and y directions respectively, $k^2 = k_x^2 + k_y^2$, and Δz is the thickness of each slice. This is approximation of tilt is valid up to about 1 degree (17 mrad)[7]. Since experimental sample mistilts are around 1 mrad, this approximation is valid.

$$P(k, \Delta z, \theta) = \exp[-i\pi\lambda k^2 \Delta z + 2\pi i \Delta z (k_x \tan\theta_x + k_y \tan\theta_y)] \tag{1.9}$$

The advantage of the propagator approach, as opposed to tilting the crystal itself, is that it allows atomic layers to be aligned to our slicing and improves the accuracy of the simulation. To achieve this same accuracy with a tilted crystal would require more slices and a higher computational overhead.

1.2.3 Frozen Phonon Approximation

It is important to account for changes in the propagation of electrons as a result of phonons in the crystal. In order to do this, I used the Frozen Phonon Approximation [19, 29]. This approximation assumes that the time scale of thermal vibrations is much larger than the time the electron spends near any given atom. If this assumption is true, we can treat the atom as stationary as the electron passes by and imitate thermal displacement by randomly displacing atoms at the start of the simulations.

Given that the beam energy of my simulations is 300 KeV, the speed of each electron is approximately 0.77c, as given by Eq. 1.10. If we estimate the period of oscillation of a phonon to be about $0.1\,\mathrm{ps}$ [24] and we know the maximum thickness of the sample to be 30nm, then the electron traverses this region in 130 attoseconds, which is much smaller than the period of oscillation, approximately a factor of 10^{-3}. Thus, for the purposes of this simulation, phonons can be treated as stationary (frozen) with high accuracy.

$$KE = (\gamma - 1)mc^2 \quad \text{where} \quad \gamma = \frac{1}{\sqrt{1 - \frac{v^2}{c^2}}} \tag{1.10}$$

Because the time the probe spends at any given position of the material is long (on the order of milliseconds) compared to the timescale of phonon vibrations, we cannot use one phonon configuration to generate STEM images. Instead, one must average several frozen phonon configurations to generate a final STEM image. The number of configurations is inversely proportional to the thickness of the sample.

1.2.4 Multislice Convergence

Insufficient sampling will result in artifacts in the image. This can manifest as displacements in atomic columns, incorrect intensities, or the appearance of non-physical features in the STEM images. An example of insufficient real space sampling is presented in Figure 1.3. Furthermore, there is no way to know *a priori* if the sampling in real and reciprocal space is sufficient before a simulation is run. However, first order multislice, the kind used for the simulations in this paper, is an unconditionally stable algorithm. Therefore, getting accurate results requires increasing sampling iteratively until a stable solution is reached. Note that while this is a necessary condition for multislice results to be accurate, it is not sufficient: it is entirely possible for the solution to converge on a stable but not physically accurate result.

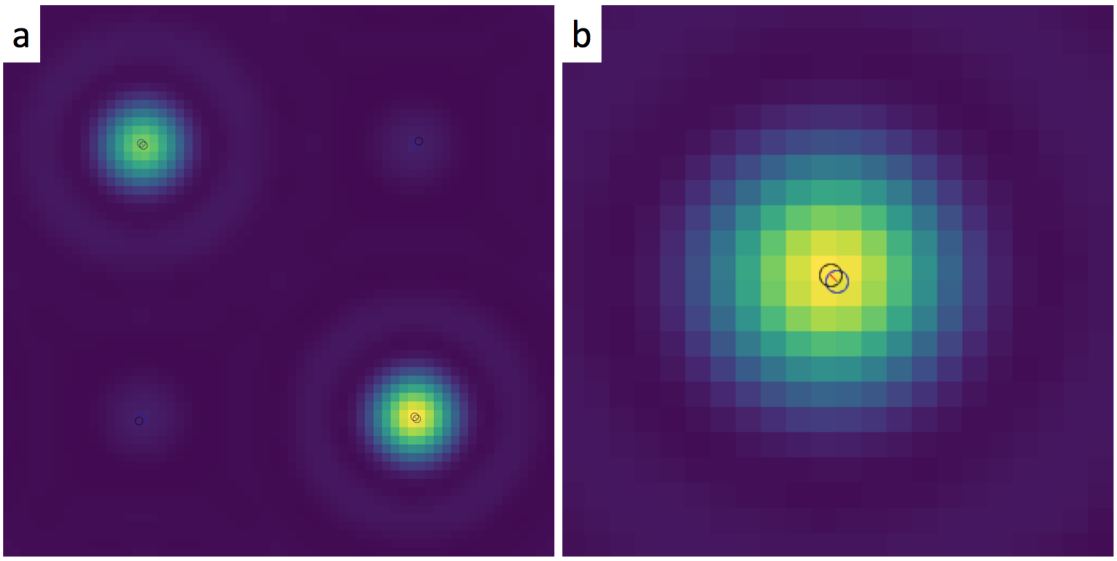

Figure 1.3: Insufficient real space sampling can result in atomic columns that are artificially displaced. In this example, real space sampling of 64x64 pixels in untilted STO results in a 2.2 picometer shift of all atoms toward the center of the image. Image a) gives a view of entire unit cell, whereas b) zooms in on the strontium column in the bottom right quadrant to highlight the artifact. The small blue circle in b) shows the correct center of the column and the small black circle shows the fitted location.

CHAPTER 2

METHODS

2.1 Methods Overview

In order to understand the effect of tilt on ABF and HAADF image formation in STO, I simulated STEM images at various tilt angles and thicknesses. To demonstrate the effects with phonons, I performed simulations which averaged over configurations with artificial displacements in the lattice. To do this I built a multislice simulation pipeline, which works by specifying parameters of interest, passing them to code which launches autostem instances, processes the results, and then generates graphs of the final values. A graphical description of the simulation and analysis pipeline is presented in Figure 2.1.

2.2 Input file

Autostem takes both microscope parameters and sample parameters as inputs. Microscope parameters are supplied directly to the program via a command line interface (CLI). They include the probe aperture, probe aberrations, defocus, and lens aberrations. To allow me to perform hundreds of runs of the program automatically, I specify these values via a metadata file written using JavaScript Object Notation (JSON) which allows the program to generate the CLI inputs automatically. An example can be found in Appendix A.

The benefits of having a dedicated input file (as opposed to directly writing input into autostem) are multifold. First, the file gives a human readable and

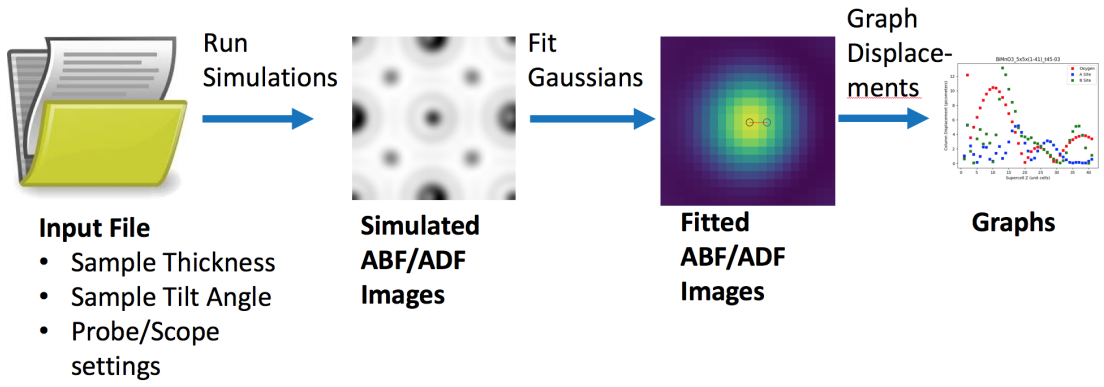

Figure 2.1: Depiction of the multislice processing pipeline.

editable document of the parameters used in simulation. Second, the file is used by the data processing code to determine how to analyze and organize the results. A major perk of this is that a user can change the values in the input file to be a subset of the ones used in simulation, allowing a small amount of data be analyzed at a time. Lastly, the input file format allows the specification of ranges which should be simulated. For example, one can specify a range of sample tilt values, and then launch an autostem instance for each value.

2.3 .xyz File

The sample unit cell is specified via an .xyz file, which is replicated in all 3 dimensions by Autostem to create the full sample. All simulations in this paper use STO, and the .xyz file is included in Listing 2.1.

```
SrTiO3 Simulation
   3.905    3.905    3.905
38 1.9525   1.9525   1.9525   1.0   0.0887
22 0.0      0.0      0.0      1.0   0.0746
8  1.9525   0.0      0.0      1.0   0.0963
8  0.0      1.9525   0.0      1.0   0.0963
8  0.0      0.0      1.9525   1.0   0.0963
-1
```

Listing 2.1: STO .xyz file used in my simulations. First Line: Comment Line. Second Line: Unit cell size in Angstroms in x, y, and z directions respectively. Further lines: Location of each atom, specified by the atomic number, x, y, z position, the probability of it being there (for materials with mixed elements), and the standard deviation of its thermal oscillations. Final Line: -1, to indicate end of file.

2.4 Scripts

My approach required me to run hundreds of multislice simulations. As such, manually editing and rerunning the inputs each time would not be practical. In order to perform large numbers of simulations on a variety of tilt and thickness configurations, I wrote a couple of python scripts which automate the generation of input to multislice and the organization and processing of the results.

The scripts are as follows:

- **runjobs**: Reads in an input file, creates the necessary autostem input files needed to run the simulations, and then launches the simulations.

- **processresults**: Once simulations are complete, this is run in the folder with the results, taking the input file as an argument. It organizes the output simulation files, fits them, and generates graphs and a dictionary of the fit.

Both scripts have backend python libraries that do much of the heavy lifting.

Even with the automation of the scripts, the simulations required substantial computing power. To accommodate this I used the Institute for Computational Science and Engineering (ICSE) computing cluster at Cornell University. The runjobs script has the ability to launch distributed instances of Autostem as required. This allowed me to run Autostem over hundreds of configurations over a few months using hundreds of distributed CPUs, which would take years to run locally on a single CPU.

2.5 Image Fitting

Once the simulations were complete, to find the locations of atoms, I used Gaussian fitting of the atomic peaks in both the ABF and HAADF images. I performed fitting using the Mixture of Gaussian (MOG) [6] fitting framework, which fits Gaussians to an image using the LGMRES linear optimization algorithm [2]. Eq. 2.1 gives the 2D Gaussian function, where the A, x_0, y_0, s_x, and s_y parameters are optimized to minimize differences with the input image.

$$f(x,y) = A \exp\left(-\left(\frac{(x-x_o)^2}{2\sigma_x^2} + \frac{(y-y_o)^2}{2\sigma_y^2}\right)\right). \tag{2.1}$$

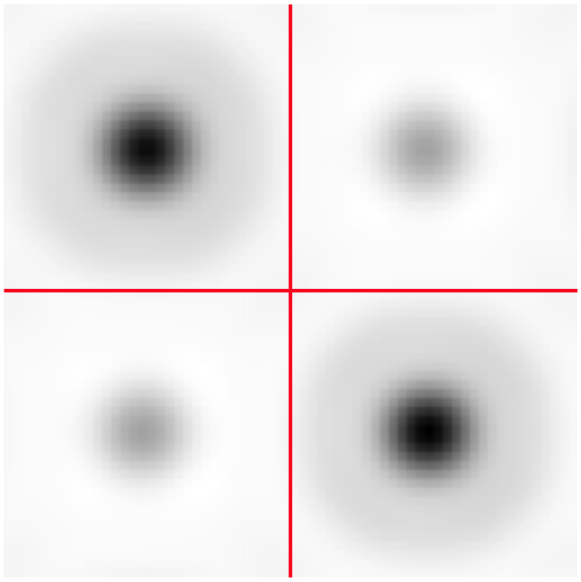

Figure 2.2: A unit cell is split into quadrants, with an atomic column centered in each one.

2.5.1 Fitting Procedure

First, I shifted the image such that each atom was centered within a quadrant of the image. Each quadrant had exactly one column and that column was centered in a zero tilt image. Each quadrant is then re-normalized to enhance contrast. I did this because in both HAADF and ABF images the strontium columns are much brighter than the titanium/oxygen columns, and the titanium/oxygen columns brighter yet than the oxygen columns. As such the linear optimizer struggles to fit the oxygen peaks if the image is not partitioned in this manner because the strontium peak dominates the signal. Figure 2.2 shows an example of how the slicing is done.

To fit the atoms, I start with the center of each quadrant as a guess for the linear solver. Then, as I increment the tilt, I use the previous result a my starting point for the next fit, e.g. using a 4 mrad tilt peak as the starting point for the

5 mrad peak at the same thickness. Despite the sometimes dramatic shifts that developed at higher tilt angles, this iterative approach allowed me to fit atoms well enough that I was unable to find any fitting error through visual inspection.

The displacement of the atom from the center of the quadrant is a direct measure of the tilt induced displacement, since columns that have no tilt or phonons will be centered. I present an illustration of measuring displacements relative to this location in Figure 2.3. The vertical banding through the center of each atom, most visible on the left two atoms, is a stitching artifact from shifting atoms away from the edges of the image. Despite the fact that this image has no phonons, banding is present because I under-sampled the image in real space. Higher sampling is needed to eliminate this artifact.

2.5.2 HAADF vs. ABF Fitting

In simulated HAADF images, Gaussian fitting successfully fit all strontium and titanium peaks. Oxygen atoms would not be visible in experimental HAADF images, so I didn't fit them. Over the full range of sample tilts and thicknesses the atomic column peaks remained Gaussian.

Simulated ABF images were more difficult to fit. This was because the atomic columns had an Ares-disk like pattern with several bands switching from light to dark. This banded structure is not as problematic when fitting experimental images due to blurring induced by lower resolution per atom, experimental noise, probe aberrations, and defocus. This blurring tends to make the atoms appear as a spot of one color.

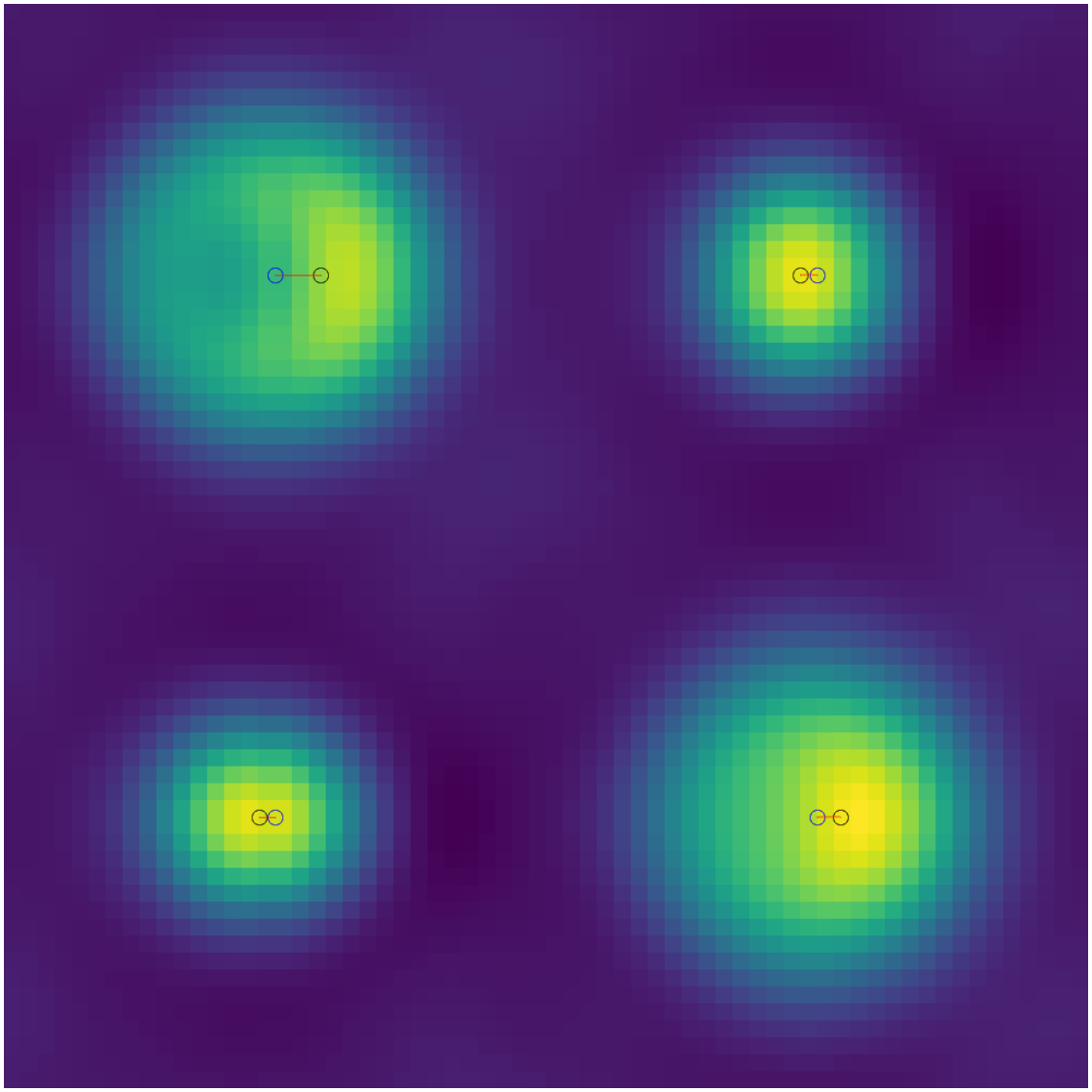

Figure 2.3: Simulated $8.6\,\mathrm{nm}$ thick (22 unit cell) STO ABF image with 2 mrad sample tilt. The blue circles indicate the center of the quadrant (equivalently the zero-tilt atomic column location), the black circles represent the fitted location. The red line between these circles is the displacement vector. Note that the oxygen columns (top right and bottom left) are displaced in the opposite direction as the cation columns (titanium/oxygen top left, strontium bottom right).

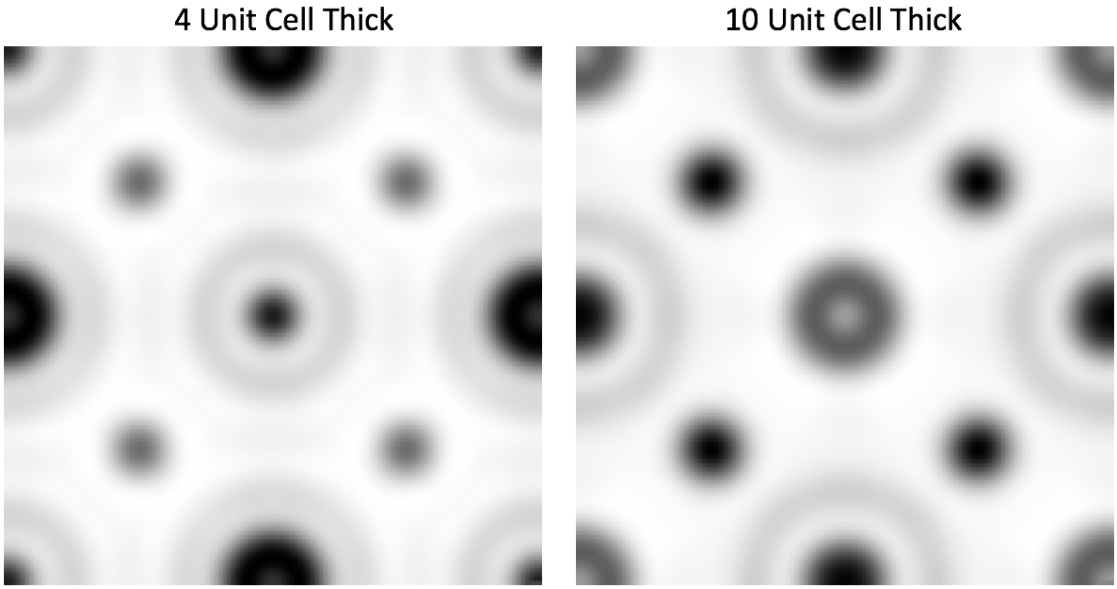

Figure 2.4: Contrast inversions occur in ABF-STEM images as thickness changes. Both images are simulated cubic $BiMnO_3$ with STO lattice spacing, no sample tilt, no phonons, no aberrations, no defocus (focus set to center of the sample), $300\,\mathrm{keV}$ beam energy, $21.4\,\mathrm{mrad}$ of aperture, and ABF detector angles of $10.7\,\mathrm{mrad}$ to $21.4\,\mathrm{mrad}$. The manganese/oxygen columns are at the center and corners of the images. The bismuth column is centered on the edges the images.

Because the ABF detector sits in the path of the electron beam as it exits the sample, it collects unscattered electrons. This means that phase information is present in ABF images. A direct consequence of this is that as sample thickness changes, the atomic columns invert contrast in ABF images, as seen in Figure 2.4. These inversions make atomic columns more difficult to fit with a simple Gaussian model. Furthermore, sample tilt causes large distortions in the shape of the peak, making them asymmetric, as seen in Figure 2.5.

Due to these factors, I had less success fitting ABF images than fitting HAADF images. Fitting the ABF images using more sophisticated models than a simple Gaussian would have mitigated this somewhat. However, in experi-

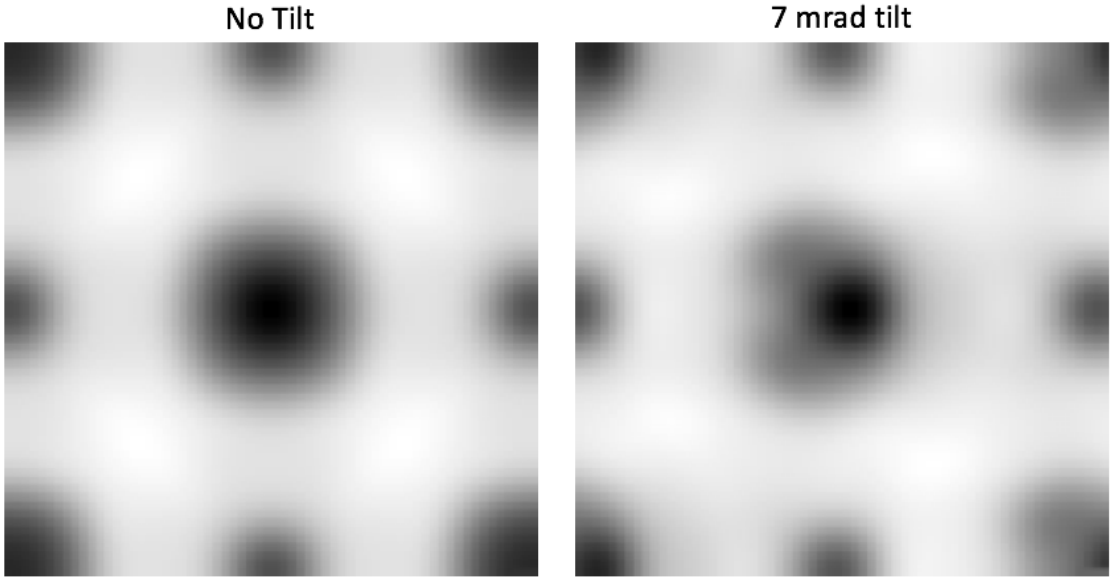

Figure 2.5: Atomic columns in ABF-STEM images become less Gaussian in shape as sample tilt increases. Both images are $15\,\mathrm{nm}$ thick (39 unit cell) simulated cubic STO with no phonons, no aberrations, no defocus (focus set to center of the sample), $300\,\mathrm{keV}$ beam energy, $21.4\,\mathrm{mrad}$ of aperture, and ABF detector angles of $10.7\,\mathrm{mrad}$ to $21.4\,\mathrm{mrad}$. The strontium column is located at the center of the images, and titanium/oxygen columns are located at the corners.

ment they are well fit by a Gaussian, and I wanted to mimic experimental analysis as closely as possible. Despite these challenges, I was able to extract a clear trend line in the data. That said, the ABF results should be treated as having a substantially larger margin of error due to fitting than the HAADF images. The exact magnitude of this error is difficult to quantify. However, I estimate the error in HAADF fitting to be under $0.25\,\mathrm{pm}$ and error in ABF fitting to be under $1.5\,\mathrm{pm}$.

CHAPTER 3

RESULTS

3.1 Definitions

3.1.1 Tilt Angle

The sample tilt angle is defined relative to the z-axis, which is the axis of the electron beam. A tilt angle of zero mrad means the beam's axis and the sample's [0 0 1] axis are aligned. A non-zero tilt angle, unless otherwise stated, is in the $-\hat{x}$ direction. The $-\hat{x}$ direction points to the left in all images in this paper. As an example, in Miller Index notation, a tilt of 10 mrad is approximately imaging the [-0.01 0 1] axis of the crystal.

Due to the cubic symmetry of STO, a tilt in the $\hat{y}$ direction would display the same qualities as a tilt in the $\hat{x}$ direction, so simulating this is not necessary. This cubic symmetry also means that it is only necessary to simulate tilts in a $45°$ arc on the x-y plane to get a complete understanding of how the direction of the tilt affects the resulting STEM image. From my simulations, only at extreme tilt angles of $5\,\mathrm{mrad}$ or larger did the tilt direction affect the magnitude of the atomic column displacement. Because tilt can be reduced below this threshold in STEM imagining, I did not investigate the impact of the tilt direction further. However, I speculate that the change is due to the fact that it is easier for electrons to channel between atomic columns that are closer. Since columns in the $\hat{x}$ or $\hat{y}$ directions are closer by a factor of $\sqrt{2}$ than in the $(1, 1)$ direction, we would expect high-angle tilt effects to be stronger with a tilt in the $\hat{x}$ direction than in

the $(1, 1)$ direction.

3.1.2 Tilt Induced Displacement

In a $20\,\mathrm{nm}$ thick sample with $1\,\mathrm{mrad}$ of sample tilt, the difference in atomic position in the tilt direction between the top atom and the bottom atom in any given column is $20\,\mathrm{pm}$. While this may seem small, this is substantially larger than any tilt effects I simulated in a $1\,\mathrm{mrad}$ tilted STO sample. Having the top and bottom atoms in a column change relative position based on tilt raises important concerns about where the origin of a column is in a tilted STEM image.

Fortunately, these concerns are not relevant. Having an origin to measure a column from is not necessary in an STEM image, nor does it matter if that origin changes across tilt angles. The relevant factor when measuring bond angles or oxygen displacements is the *relative* locations of neighboring strontium, titanium/oxygen, and oxygen columns. After all, a shift of every feature of the image by $20\,\mathrm{pm}$ is simply a translation of the entire image, and it does not affect the relative distances of different columns. As such, we only care about the tilt induced *distortion* in the image. Since STEM images are fitted using Gaussians, we measure this by comparing how tilt changes inter-column spacing. By measuring the impact of tilt on inter-column spacing, we quantify how tilting the sample causes STEM images to deviate from the true atomic structure.

From the symmetry of the input crystal, we expect zero displacement between all columns in an untilted crystal. This serves as a basic check on the validity of our simulation and a good way to measure sampling error. Indeed, Figure 3.1 shows that in the case without phonons, the results agree with this

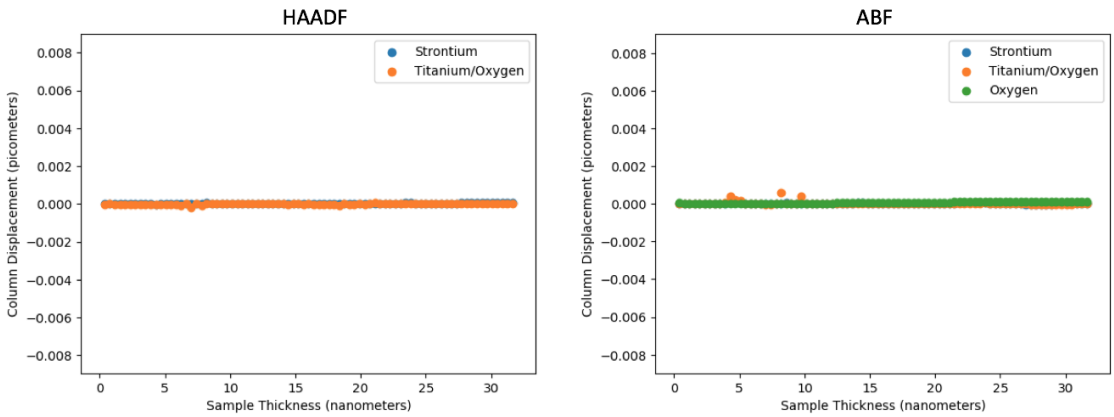

Figure 3.1: Graphs of ABF and HAADF column displacements with zero sample tilt over a range of thicknesses show no deviation from the center of the atomic column. No phonons are included. The label "Titanium/Oxygen" is used because in the [1 0 0] projection of cubic STO, titanium alternates with oxygen in the column. This is not to be confused with the columns of pure oxygen, which are distinct.

expectation.

When not comparing two columns directly, displacement values are measured relative to the zero-tilt location for a column. While it is true that only the inter-column displacement matters, this convention helps highlight the effects of channelling and makes the graphs a bit easier to read.

As a matter of convenience, all tilt-induced displacements are listed as signed scalars. As discussed in Section 3.1.1, unless otherwise stated all tilts and displacements are in the $-\hat{x}$ direction. I use positive values to refer to displacements in the $-\hat{x}$ direction (leftward in an image), and negative values to refer to displacements in the $\hat{x}$ direction (rightward in an image). An important assumption underlying measuring all displacements along $\hat{x}$ is that displacements are in fact in this direction. In simulations without thermal noise, this is

guaranteed by the symmetry of the setup. In simulations with thermal noise discussed in this paper, the $\hat{y}$ component of this vector is indistinguishable from the thermal noise itself.

3.1.3 Simulation Parameters

Beam energies in all simulations are $300\,\mathrm{keV}$. All simulations discussed are with no lens aberrations and no defocus (meaning the focal point is the center of the sample). While Gao et al. showed variations in defocus and aperture to have a substantial impacts on tilt induced column displacement in ABF [11], the impact of these parameters is not investigated in this paper.

3.2 Impact of Tilt on STEM Images

The location of atomic columns in ABF-STEM images is highly sensitive to sample tilt of even a few milliradians. In the case of a tilted sample, the atomic columns remain well defined, but are translated along the direction of the tilt. However, due to channelling effects, the displacement is sometimes in the negative tilt direction. Figure 3.2 shows a demonstration of this.

Even at $1\,\mathrm{mrad}$ of sample tilt, which is difficult to avoid in an experimental setting, the displacement between the titanium/oxygen column and the oxygen column reaches $11.8\,\mathrm{pm}$ and the difference between the strontium column and the oxygen column reaches $4.2\,\mathrm{pm}$. This difference varies strongly with thickness. Figure 3.3 shows the dependence.

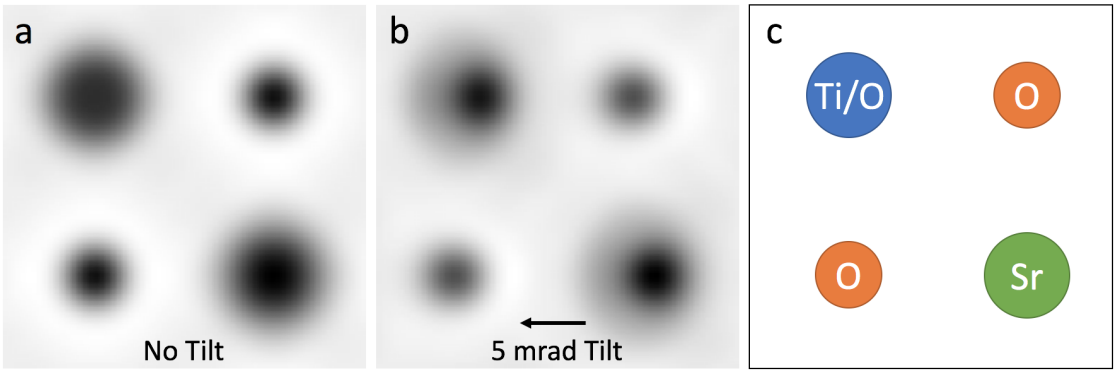

Figure 3.2: Tilt effects can cause substantial dislocations of atomic columns in both directions along the tilt axis. The ABF images are of simulated $8\,\mathrm{nm}$ thick (20 unit cells) STO a) with no sample tilt and b) with $5\,\mathrm{mrad}$ sample tilt. c) Atomic column legend. In the tilted sample, the oxygen columns are displaced in the opposite direction as the titanium/oxygen and strontium columns.

The effect becomes more extreme at higher tilt angles. However, even at $1\,\mathrm{mrad}$ of tilt the effect is pronounced enough to make reliable picometer-scale measurement of relative column locations impossible.

HAADF images are much less susceptible to tilt effects. Because oxygen atoms are not visible, we only need to investigate the relative displacement between the strontium and titanium/oxygen columns. Figure 3.4 shows that even with extreme tilt angles of 10 mrad, the displacement between strontium and titanium/oxygen columns is under $2\,\mathrm{pm}$. I present a direct comparison to ABF tilts over the same range in Figure 3.5 to show the dramatic difference in the tilt induced displacement between the detectors.

The HAADF-ABF comparison also highlights, that at thicknesses of 6 unit-cells or less, the tilt induced displacements are qualitatively similar to each other. In this region in both ABF and HAADF STEM, the tilt induced displacement is linearly proportional to the tilt angle, which is not true generally (See

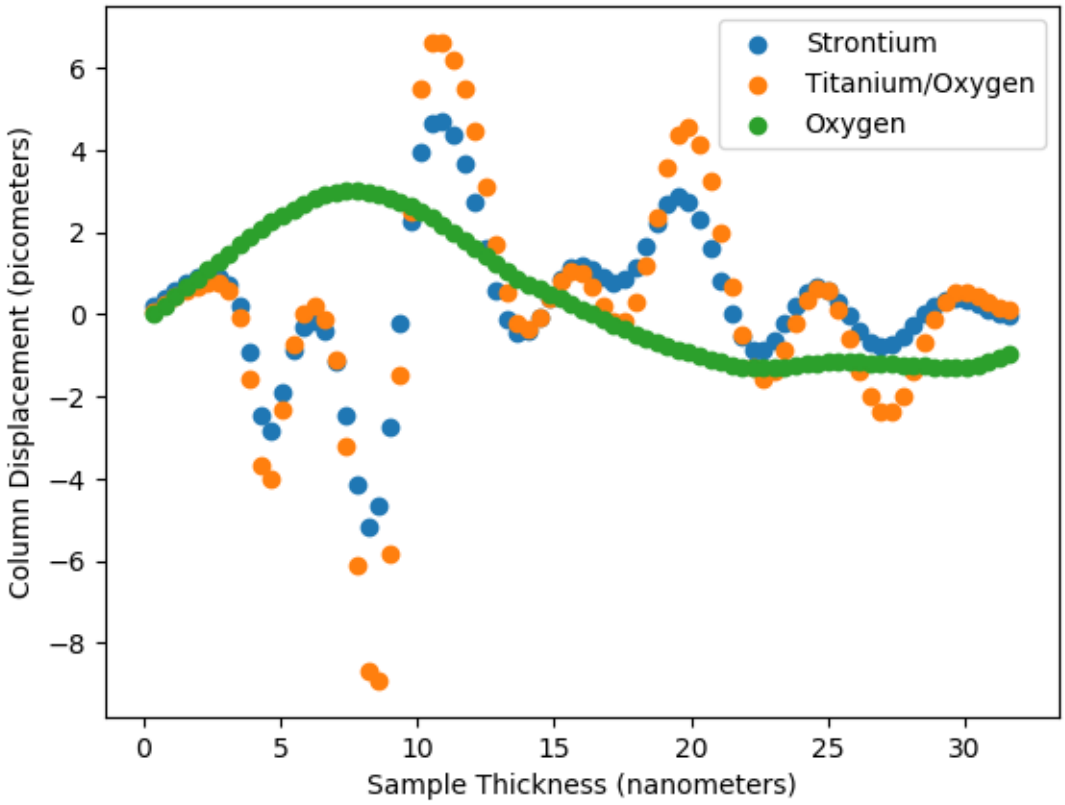

Figure 3.3: A plot of the tilt induced column displacement in simulated $1\,\mathrm{mrad}$ tilted STO shows that tilt effects are substantial even at small tilt angles. Worse, the oxygen column is not in phase with the cation columns, leading to additive error. The oscillations of the displacements are caused by electron channeling effects.

Figure 3.6). I suspect the reason for this linear relationship is because at these thicknesses, channelling effects are effectively linear. I arrived at this supposition by modelling channelling effects in a simple classical picture as simple harmonic oscillations of the electron beam around the nuclear potentials in the atomic column in the $-\hat{x}$ direction. By setting the initial position to zero and the initial (tilt-induced) velocity to $-V_x$, the electron's x position is given by Eq. 3.1. This means that for a short time after $t = 0$, the electron should be offset linearly with time (and therefore thickness) before settling into oscillatory motion, which is what we see in Figure 3.6.

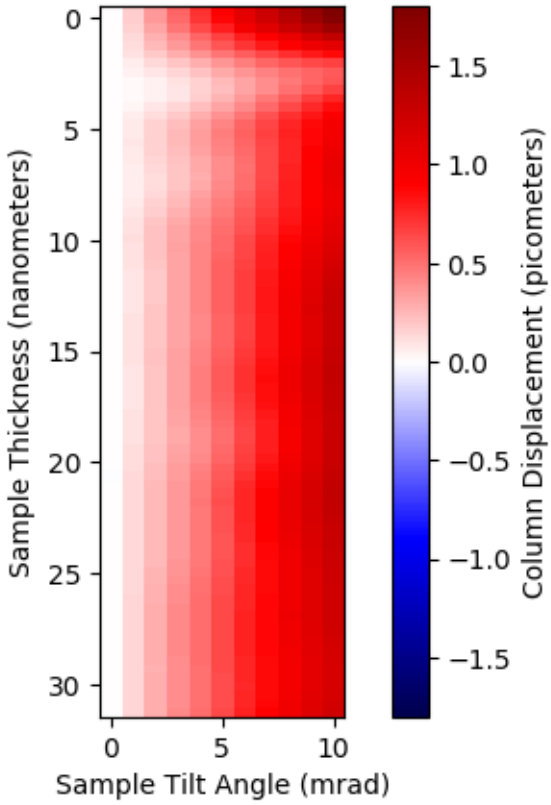

Figure 3.4: HAADF-STEM is robust to high degrees of sample tilt. Even at tilts of $10\,\mathrm{mrad}$, displacements never exceed $2\,\mathrm{pm}$. The plot shows the tilt-induced displacement between strontium and titanium/oxygen columns as a function of sample thickness (vertical axis) and tilt angle (horizontal axis) in cubic STO simulated without phonons.

$$x(t) = -V_x \sin(wt) \tag{3.1}$$

3.3 Phonon Results

Using the frozen phonon approximation discussed in Section 1.2.3, I ran simulations over the same range of thicknesses and tilt angles to see how they affected

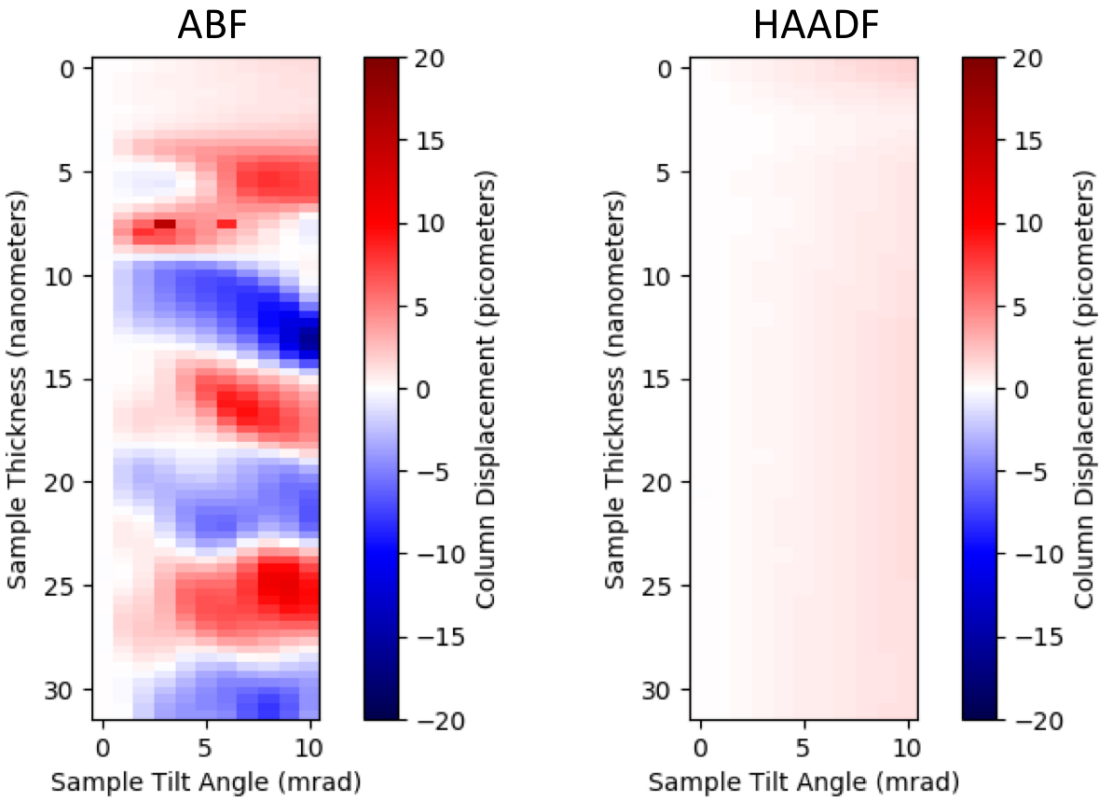

Figure 3.5: HAADF-STEM is substantially less sensitive to sample tilt than ABF-STEM. Tilt-induced displacement between strontium and titanium/oxygen columns in simulated ABF-STEM (left) and HAADF-STEM (right) for STO highlight the difference. Both plots are on the same scale.

the results. The results with phonons were very similar to the results without phonons, and a comparison of ABF results is presented in Figure 3.7. Despite significant noise, there appears to be a trend where the introduction of phonons reduces the frequency of tilt induced beam oscillations about the atomic column centers.

Another important result from Figure 3.7 is that there are no clear thickness or tilt regimes where displacement is minimized. In the phonon-free results there are specific thicknesses which appear to have zero displacement.

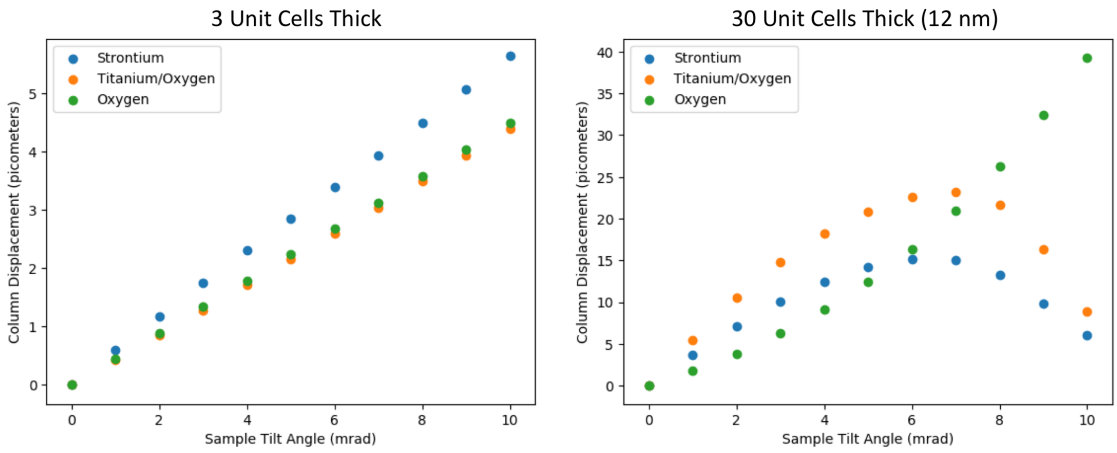

Figure 3.6: Left: At low thicknesses (3 unit cells) tilt-induced column displacement in simulated ABF-STEM is linearly related to the tilt angle. Right: At high thicknesses ($12\,\mathrm{nm}$) the dependence is nonlinear and not easily modelled in a general way. The qualitative behavior of the curve varies dramatically with thickness.

However, the presence of phonons changes these thicknesses. One can reasonably assume that experimental variation would also affect the location of these displacement-free regions, making it impossible to confidently target them experimentally.

The significant noise and poor fitting in the phonon image is the result of insufficient numbers of phonon configuration and insufficient real space simulation sampling. Additionally, the titanium/oxygen column and oxygen columns are poorly fit, as they are stitched-together versions of multiple atoms which were averaged over different phonon configurations due to their placement on the edge of the unit cell. These "frankenatoms" are not physically realistic, and thus the results are not as accurate. Figure 3.8 presents an example.

In order to properly investigate the effects of phonons, I will need to re-run these simulations with more phonons, especially including more phonon con-

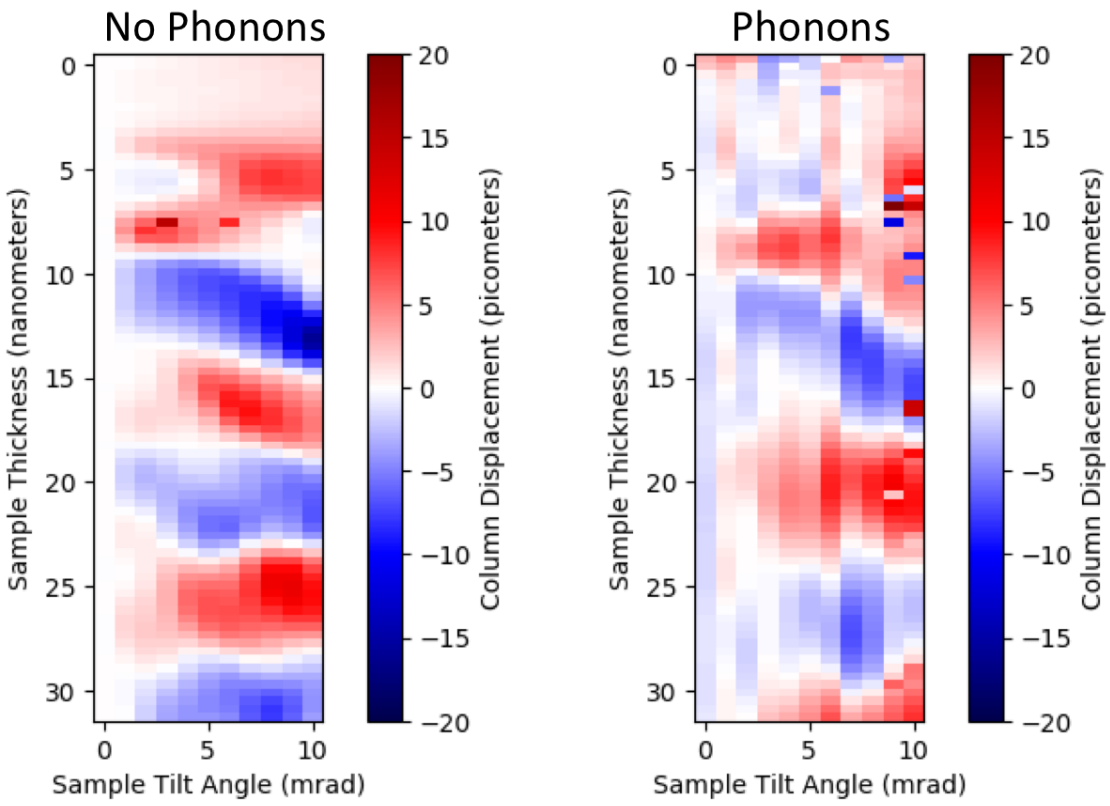

Figure 3.7: The frequency of the oscillation of the tilt-induced displacement between strontium and titanium/oxygen columns as a function of thickness changes when phonons are added. However, the qualitative behavior of the system remains the same. Simulated STO ABF-STEM is presented without phonons (left) and with phonons (right). In the phonon image, each vertical band represents the average of 16 distinct phonon configurations.

figurations at lower thicknesses. Additionally, the atoms will need to be located away from the edges of the unit cell to ensure they are not stitched together versions of different atoms. Due to substantial computational requirements, these images were not generated for this paper.

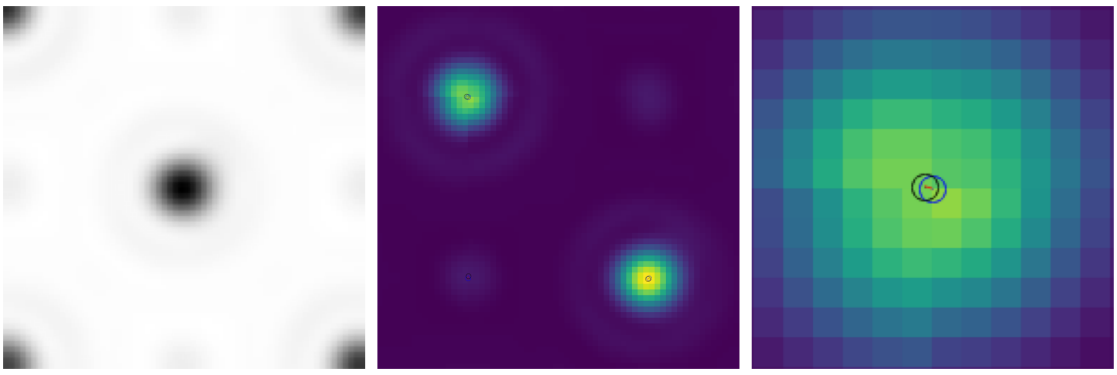

Figure 3.8: When an atom is placed on the corner of the unit cell, 4 different atoms must be stitched together. Since each atom has different phonon configurations, the result is not a cohesive atom. Left: Image before stitching. Center: Image is shifted ¼ unit cell down and right, then fitted. Right: Zoom of stitching artifacts in fitted TiO column. Images are simulated STO with 16 phonon configurations.

3.4 Evidence of Channelling

To support the hypothesis that electron channelling is the dominant source of tilt induced oscillations in STEM images, I simulated the path of the electron beam through the material. My simulations show that without tilt, the beam remains symmetric around atomic columns when centered over them. However, as tilt is added, the beam oscillates around atomic columns. Figure 3.9 shows the beam intensity profile.

3.5 Conclusions

In cubic STO, sample tilt of $1\,\mathrm{mrad}$ is sufficient to create displacements of $11.8\,\mathrm{pm}$ between titanium/oxygen and oxygen columns and $4.2\,\mathrm{pm}$ between strontium

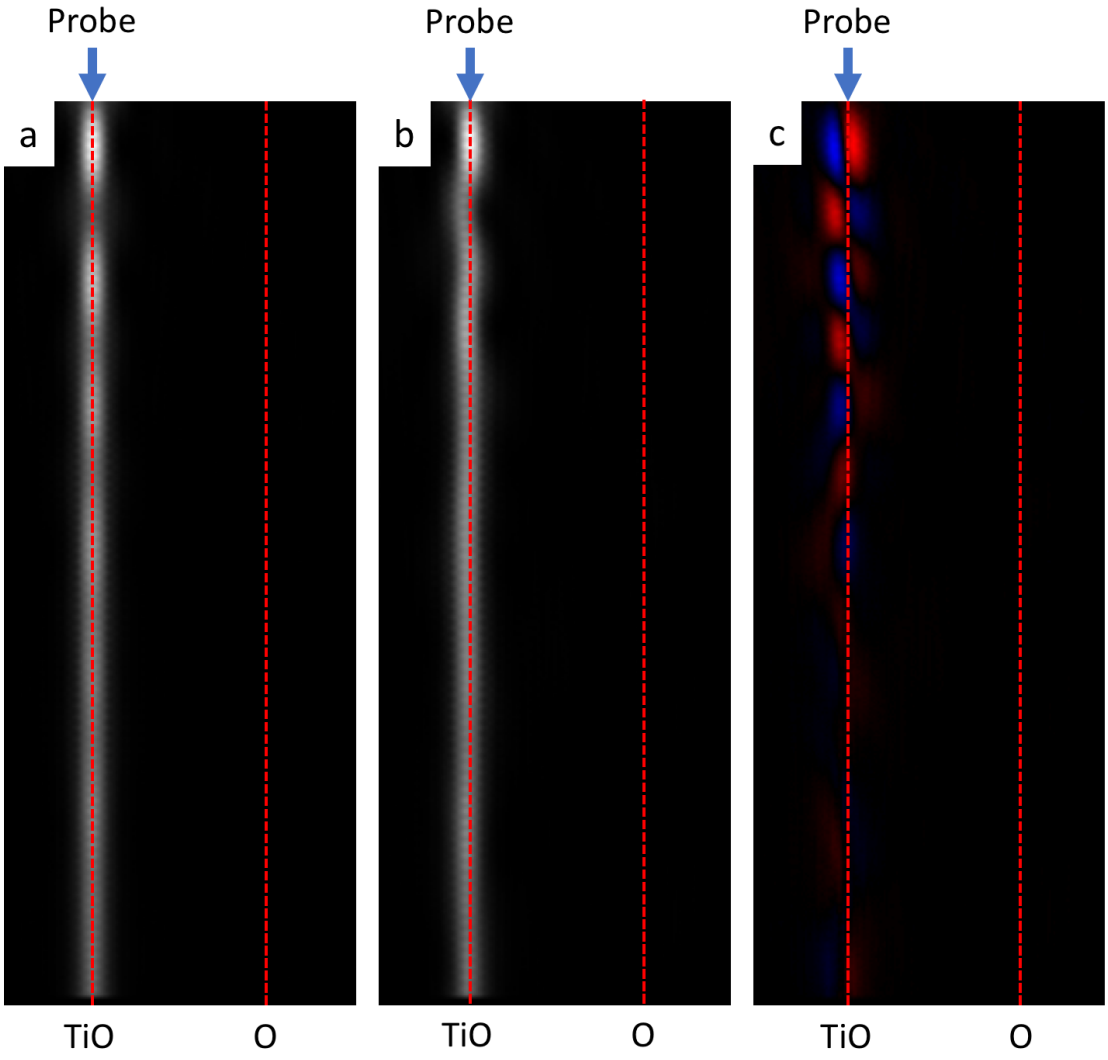

Figure 3.9: Electron channelling effects lead to oscillations of the probe around atomic columns during STEM. Image a) shows the beam centered on the TiO column in an untilted sample. It remains symmetric about the column, whereas when the sample is tilted $6\,\mathrm{mrad}$ in b) the electron probe oscillates about the TiO column. Image c) shows a color map of the difference between the untilted and $6\,\mathrm{mrad}$ tilted beam intensity profiles, which highlights the oscillatory nature of the channelling effects. Presented are images of $30\,\mathrm{nm}$ thick simulated cubic STO with no phonons, no aberrations, no defocus (focus set to center of the sample), $300\,\mathrm{keV}$ beam energy, and $21.4\,\mathrm{mrad}$ of aperture.

and oxygen columns. Sample tilts of this magnitude are extremely difficult to control for or detect experimentally especially for large convergence angles, even with the use of CBED alignment. There appear to be no thickness regimes where this effect is consistently or predictably not present. Consistent with the conclusions of Zhou and Gao [11, 42], claims of picometer-scale measurements drawn from ABF-STEM imaging need to be made with caution.

My results also suggest that HAADF-STEM suffers from less than $2\,\mathrm{pm}$ of tilt-induced displacement at tilts of $10\,\mathrm{mrad}$ for samples as thick as $30\,\mathrm{nm}$. As such, cross-referencing cation positions between ABF and HAADF imaging can be used to mitigate tilt risk. If cation positions differ substantially between the two imaging modes, then tilt is likely having a strong effect on the quality of ABF measurements and measurements with lower tilt angles should be taken. However, as my results show, good agreement is no guarantee of perfect alignment, as the tilt effects on oxygen and cation columns do not correlate with each other.

Ultimately, my results show that the goal of measuring all atomic columns in a crystal with sub-picometer accuracy remains elusive using current STEM imaging techniques. Microscopers need to be able to consistently align sample lattices to the beam with sub-milliradian precision if they want to make picometer-scale claims about atoms in materials not visible using HAADF-STEM. Alternatively, while difficult and time consuming, averaging over several randomized ABF images could allow microscopers to determine tilt-induced variation and hone in on the true atomic structure.

APPENDIX A

CODE

Listing A.1: Example input file

```
{
"material": "STO",
"unitcell_size": [3.905, 3.905, 3.905],
"site_names": ["strontium", "titanium", "oxygen"],
"site_counts": [1, 1, 2],
"unitcell_atomic_pos": [[0.5, 0.5],
                        [0.0, 0.0],
                        [0.5, 0.5], [0.0, 0.5]],
"slices_per_unitcell": 6,
"generate_cbed": false,
"thermal_configs": 16,
"realspace_size_x_pixels": 256,
"enable_xzmode": true,
"unitcell_y_xzmode": 0.5,
"abf_inner_angle_mrad": 10.7,
"abf_outer_angle_mrad": 21.4,
"supercell_x_range": {
    "value": 5
},
"supercell_y_range": {
    "value": 5
},
"supercell_z_range": {
```

```
        "start": 1,
        "end": 81,
        "step": 1,
        "range_type": "Linear"
    },
    "probe_range": {
        "value": 1024
    },
    "tilt_planar_angle_degrees_range": {
        "start": 0,
        "end": 0,
        "step": 15,
        "range_type": "Linear"
    },
    "tilt_z_angle_mrad_range": {
        "start": 0,
        "end": 4,
        "step": 1,
        "range_type": "Linear"
    },
    "displacement_range": {
        "value": null
    },
    "aperture_mrad_range": {
        "value": 21.4
    },
```

```
    "v0_kev_range": {
        "value": 300
    },
    "job_min_processors": 4,
    "job_max_processors": 4,
    "job_prefix": "quick_sto",
    "job_queue": "short"
}
```

BIBLIOGRAPHY

[1] Ryotaro Aso, Daisuke Kan, Yuichi Shimakawa, and Hiroki Kurata. Octahedral tilt propagation controlled by a-site cation size at perovskite oxide heterointerfaces. *Crystal Growth & Design*, 14(5):2128–2132, 2014.

[2] Allison H Baker, Elizabeth R Jessup, and Thomas Manteuffel. A technique for accelerating the convergence of restarted gmres. *SIAM Journal on Matrix Analysis and Applications*, 26(4):962–984, 2005.

[3] PE Batson, Niklas Dellby, and OL Krivanek. Sub-ångstrom resolution using aberration corrected electron optics. *Nature*, 418(6898):617, 2002.

[4] John C Bravman and Robert Sinclair. The preparation of cross-section specimens for transmission electron microscopy. *Microscopy Research and Technique*, 1(1):53–61, 1984.

[5] Henry N Chapman, Petra Fromme, Anton Barty, Thomas A White, Richard A Kirian, Andrew Aquila, Mark S Hunter, Joachim Schulz, Daniel P DePonte, Uwe Weierstall, et al. Femtosecond x-ray protein nanocrystallography. *Nature*, 470(7332):73, 2011.

[6] Colin Clement. Mixture of gaussian model for finding atoms in (s)tem images. `https://github.com/colinclement/mog`, 2018.

[7] John Maxwell Cowley. *Diffraction physics*. Elsevier, 1995.

[8] Albert V Crewe, M Isaacson, and D Johnson. A simple scanning electron microscope. *Review of Scientific Instruments*, 40(2):241–246, 1969.

[9] Niklas Dellby, L Krivanek, D Nellist, E Batson, and R Lupini. Progress in aberration-corrected scanning transmission electron microscopy. *Journal of Electron Microscopy*, 50(3):177–185, 2001.

[10] Harrison W Fuller and Murray E Hale. Determination of magnetization distribution in thin films using electron microscopy. *Journal of Applied Physics*, 31(2):238–248, 1960.

[11] Peng Gao, Akihito Kumamoto, Ryo Ishikawa, Nathan Lugg, Naoya Shibata, and Yuichi Ikuhara. Picometer-scale atom position analysis in annular bright-field stem imaging. *Ultramicroscopy*, 184:177–187, 2018.

[12] Joseph I Goldstein, Dale E Newbury, Joseph R Michael, Nicholas WM Ritchie, John Henry J Scott, and David C Joy. *Scanning electron microscopy and X-ray microanalysis*. Springer, 2017.

[13] David J Griffiths. *Introduction to quantum mechanics*. Cambridge University Press, 2016.

[14] Benedikt Haas, Robert A McLeod, Thomas Auzelle, Bruno Daudin, Joël Eymery, Frédéric Lançon, Jian-Min Zuo, and Jean-Luc Rouvière. Picometre-precision atomic structure of inversion domain boundaries in gan. In *European Microscopy Congress 2016: Proceedings*. Wiley Online Library, 2016.

[15] Max Haider, Harald Rose, Stephan Uhlemann, Eugen Schwan, Bernd Kabius, and Knut Urban. A spherical-aberration-corrected 200 kv transmission electron microscope. *Ultramicroscopy*, 75(1):53–60, 1998.

[16] Qian He, Ryo Ishikawa, Andrew R Lupini, Liang Qiao, Eun J Moon, Oleg Ovchinnikov, Steven J May, Michael D Biegalski, and Albina Y Borisevich. Towards 3d mapping of bo6 octahedron rotations at perovskite heterointerfaces, unit cell by unit cell. *Acs Nano*, 9(8):8412–8419, 2015.

[17] Larry Leroy Hench, R J_ Splinter, WC Allen, and TK Greenlee. Bonding mechanisms at the interface of ceramic prosthetic materials. *Journal of Biomedical Materials Research Part A*, 5(6):117–141, 1971.

[18] Richard Henderson. The potential and limitations of neutrons, electrons and x-rays for atomic resolution microscopy of unstained biological molecules. *Quarterly reviews of biophysics*, 28(2):171–193, 1995.

[19] Sean Hillyard and John Silcox. Detector geometry, thermal diffuse scattering and strain effects in adf stem imaging. *Ultramicroscopy*, 58(1):6–17, 1995.

[20] Gene E Ice, John D Budai, and Judy WL Pang. The race to x-ray microbeam and nanobeam science. *Science*, 334(6060):1234–1239, 2011.

[21] KAZUO Ishizuka and NATSU Uyeda. A new theoretical and practical approach to the multislice method. *Acta Crystallographica Section A: Crystal Physics, Diffraction, Theoretical and General Crystallography*, 33(5):740–749, 1977.

[22] Daisuke Kan, Ryotaro Aso, Riko Sato, Mitsutaka Haruta, Hiroki Kurata, and Yuichi Shimakawa. Tuning magnetic anisotropy by interfacially engineering the oxygen coordination environment in a transition metal oxide. *Nature materials*, 15(4):432, 2016.

[23] Earl J Kirkland. *Advanced computing in electron microscopy*. Springer Science & Business Media, 2010.

[24] Charles Kittel, Paul McEuen, and Paul McEuen. *Introduction to solid state physics*, volume 8. Wiley New York, 1996.

[25] Alexander V Kvit, Jie Feng, Chenyu Zhang, Dane Morgan, and Paul M Voyles. High-precision stress mapping and defect characterization of thin films of lamno 3 grown on dysco 3 substrate. *Microscopy and Microanalysis*, 22:1526, 2016.

[26] DJ Larson, DT Foord, AK Petford-Long, H Liew, MG Blamire, A Cerezo, and GDW Smith. Field-ion specimen preparation using focused ion-beam milling. *Ultramicroscopy*, 79(1-4):287–293, 1999.

[27] Zhaoliang Liao, Mark Huijben, Z Zhong, N Gauquelin, S Macke, RJ Green, S Van Aert, J Verbeeck, G Van Tendeloo, K Held, et al. Controlled lateral anisotropy in correlated manganite heterostructures by interface-engineered oxygen octahedral coupling. *Nature materials*, 15(4):425, 2016.

[28] Ariel Lipson, Stephen G Lipson, and Henry Lipson. *Optical physics*. Cambridge University Press, 2010.

[29] Russel F Loane, PeiRong Xu, and John Silcox. Thermal vibrations in convergent-beam electron diffraction. *Acta Crystallographica Section A: Foundations of Crystallography*, 47(3):267–278, 1991.

[30] SE Maccagnano-Zacher, KA Mkhoyan, EJ Kirkland, and J Silcox. Effects of tilt on high-resolution adf-stem imaging. *Ultramicroscopy*, 108(8):718–726, 2008.

[31] G McMullan, AR Faruqi, and R Henderson. Direct electron detectors. In *Methods in enzymology*, volume 579, pages 1–17. Elsevier, 2016.

[32] Douglas B Murphy. *Fundamentals of light microscopy and electronic imaging*. John Wiley & Sons, 2002.

[33] Richard Neutze, Remco Wouts, David van der Spoel, Edgar Weckert, and Janos Hajdu. Potential for biomolecular imaging with femtosecond x-ray pulses. *Nature*, 406(6797):752, 2000.

[34] Kenji Nomura, Hiromichi Ohta, Kazushige Ueda, Toshio Kamiya, Masahiro Hirano, and Hideo Hosono. Thin-film transistor fabricated in single-crystalline transparent oxide semiconductor. *Science*, 300(5623):1269–1272, 2003.

[35] Sergey V Ovsyannikov, Artem M Abakumov, Alexander A Tsirlin, Walter Schnelle, Ricardo Egoavil, Jo Verbeeck, Gustaaf Van Tendeloo, Konstantin V Glazyrin, Michael Hanfland, and Leonid Dubrovinsky. Perovskite-like mn2o3: A path to new manganites. *Angewandte Chemie International Edition*, 52(5):1494–1498, 2013.

[36] DH Shin, EJ Kirkland, and J Silcox. Annular dark field electron microscope images with better than 2 å resolution at 100 kv. *Applied physics letters*, 55(23):2456–2458, 1989.

[37] Yongwen Tan, Pan Liu, Luyang Chen, Weitao Cong, Yoshikazu Ito, Jiuhui Han, Xianwei Guo, Zheng Tang, Takeshi Fujita, Akihiko Hirata, et al. Monolayer mos2 films supported by 3d nanoporous metals for high-efficiency electrocatalytic hydrogen production. *Advanced Materials*, 26(47):8023–8028, 2014.

[38] Yi Wang, Ute Salzberger, Wilfried Sigle, Y Eren Suyolcu, and Peter A van Aken. Oxygen octahedra picker: a software tool to extract quantitative information from stem images. *Ultramicroscopy*, 168:46–52, 2016.

[39] David B Williams and C Barry Carter. The transmission electron microscope. In *Transmission electron microscopy*, pages 3–17. Springer, 1996.

[40] Z Yu, DA Muller, and J Silcox. Effects of specimen tilt in adf-stem imaging of a-si/c-si interfaces. *Ultramicroscopy*, 108(5):494–501, 2008.

[41] Qing-Hua Zhang, Dong-Dong Xiao, and Lin Gu. Aberration-corrected scanning transmission electron microscopy for complex transition metal oxides. *Chinese Physics B*, 25(6):066803, 2016.

[42] Dan Zhou, Knut Müller-Caspary, Wilfried Sigle, Florian F Krause, Andreas Rosenauer, and Peter A van Aken. Sample tilt effects on atom column position determination in abf–stem imaging. *Ultramicroscopy*, 160:110–117, 2016.